

<https://doi.org/10.1038/s40494-026-02447-1>

The effect of temperature on the development of surface deterioration on the petroglyph-bearing rocks with black crust

Changyu Wu¹, Chengyu Liu^{2,3} ✉, Jinhua Wang⁴, Xiaowei Dong⁵ & Xiangxiang Zhang²

Petroglyph-bearing rock surfaces are commonly covered by a black crust, which often detaches from the bedrock through blistering and scaling, resulting in the loss of valuable cultural information. This study, for the first time, links the petroglyph deterioration with black crust, weak interlayer, and thermal effect based on field statistical results of petroglyph deterioration development and orientation. Laboratory experiments are conducted to examine the differences in ultrasonic velocity and thermodynamic properties between the black crust and the underlying rock layers (weak interlayer and fresh bedrock). Based on the experimental results, numerical simulations are used to explore the effect of temperature on the development of blistering and scaling beneath the black crust. The results demonstrate that the development of blistering and scaling on petroglyph-bearing rock surfaces is attributed to the mismatch in thermodynamic properties between the weak interlayer and its adjacent layers.

Petroglyphs constitute one of humanity's most significant forms of cultural heritage and have been discovered on every continent except Antarctica¹. According to data from the Italian Centro Camuno di Studi Preistorici, approximately 150 major petroglyph regions have been identified worldwide to date, with more than 68,000 documented petroglyph sites and over 74 million recorded petroglyph images². A significant proportion of these petroglyphs are located in arid regions, including the Sahara in Africa, the Arabian Peninsula in West Asia, the Central Asian Plateau, and the interior of Australia^{3–7}. Because petroglyphs are predominantly exposed in desert environments, prolonged exposure to harsh natural conditions frequently leads to surface blistering, which subsequently develops into scaling, causing irreversible loss of cultural information^{8–10}.

Similar to the arid environments in which most petroglyphs around the world are found, the Damaidi petroglyph site is situated along the transitional zone between semi-desert and desert. Consequently, severe surface deterioration has developed on the Damaidi petroglyph. During the deterioration survey at the Damaidi petroglyph site, the research team observed that the blistering and scaling on the petroglyph-bearing rock surface primarily occurred on rock surfaces covered with black crust. After the black crust detached, a weak interlayer with lower mechanical strength was

exposed on the underlying bedrock surface. The corresponding field images are detailed in Section of *Peterioration phenomena*. Experimental results demonstrate significant differences in the thermodynamic properties between the black crust and its underlying rock layers (further detailed in Section of *Differences in Thermodynamic Properties between the Black Crust and Underlying Rock Layers*). In addition, field statistics indicate that petroglyph-bearing rock surfaces receiving longer durations of solar exposure are more susceptible to developing blistering or scaling (further detailed in Section of *Relationship between the Development of Blistering and Scaling and the Orientation of Petroglyph-bearing Rocks*).

In academia, the substance formed on rock surfaces over long periods of exposure to surface weathering environments, which alters the color and surface characteristics of the bedrock, is commonly referred to as rock varnish. Due to its widespread distribution in arid climatic environments, it is also referred to as desert varnish by some researchers^{11–13}. Previous studies have indicated that rock varnish typically presents as a micron-scale black coating with thicknesses ranging from approximately 20–200 μm ^{14–16}. However, the thickness of the slab-like rock layers that detach from the petroglyph surface is typically in the millimeter range, or even close to centimetres. It is evident that the rock

¹College of Civil Engineering, Fuzhou University, Fuzhou, China. ²College of Zijin Geology and Mining, Fuzhou University, Fuzhou, China. ³Research Center of Geological Engineering, Fuzhou University, Fuzhou, China. ⁴Department of Cultural Heritage and Museology, Fudan University, Shanghai, China. ⁵Liaoning Non-ferrous Geological Exploration and Research Institute Co., Ltd., Shenyang, China. ✉e-mail: Liuchengyuphd@163.com

varnish on the petroglyph surface does not represent the structure of these slab-like rock layers. Some researchers refer to the rock within a certain thickness range directly beneath the rock varnish as the modified zone or hardened layer. Studies have also found that beneath this modified zone or hardened layer, there exists a detachment zone with relatively weaker tensile strength^{17,18}. Dorn et al.¹⁹ pointed out that the case hardening is the process by which the outer shell of an exposed rock surface hardens due to near-surface diagenesis, and emphasized that rock varnish and the case hardening are two distinct phenomena. Although there has been some research on the rock varnish and hardened layer of rock surfaces, no studies have yet explored the differences in properties between the slab-like detached layer on the petroglyph surface and the underlying rock layers, nor the relationship between these structural characteristics and the development of petroglyph deterioration.

Current research on the deterioration of petroglyph-bearing rock surfaces has mainly focused on freeze–thaw processes^{20–24}. Previous studies have demonstrated a close relationship between temperature variations and surface scaling in rocks, with cyclic thermal stress potentially playing a dominant role, especially in arid environments^{25–30}. For example, Eppes et al.^{31,32} demonstrated through continuous monitoring of acoustic emissions, temperature, strain, and other environmental conditions in sun-exposed granite boulders that insolation-related thermal stresses by themselves are of sufficient magnitude to facilitate incremental subcritical crack growth, thereby making rocks more susceptible to cracking triggered by added stress from other weathering mechanisms. In addition, Collins et al.^{33,34} evaluated granite exfoliation under cyclic thermal effects using thermodynamics, structural beam theory, and fracture mechanics. The study showed that temperature variations caused by solar radiation are sufficient to trigger further fracture propagation parallel to the rock surface, ultimately leading to seemingly spontaneous exfoliation, thereby demonstrating that thermal stress plays a critical role in triggering exfoliation. Similarly, Lamp et al.³⁵ verified the potential role of thermal stress weathering in the flaking of millimeter-thick alteration rinds of Antarctic rocks through field measurements, laboratory analyses, and numerical modeling. Thermal stress models incorporating subcritical crack growth theory indicate that the thermal stresses generated at the base of thin alteration rinds are sufficient to trigger crack growth under present climatic conditions, eventually leading to rind detachment.

Although previous studies have investigated the phenomenon of rock surface detachment caused by thermal effects through field monitoring and theoretical analyses, and have achieved meaningful progress, the structural characteristics of rock surface layers were not considered in these investigations. Based on preliminary statistical analyses, this study investigates the property differences between the black crust and the underlying weak interlayer on the Damaidi petroglyph-bearing rock, and examines how these differences influence the development of blistering and scaling on the petroglyph-bearing rock surface under thermal effects. This study is not only of significant importance for the treatment of deterioration and the long-term preservation of petroglyphs, but also provides valuable guidance for understanding rock surface delamination exhibiting similar structures in arid regions.

Based on these considerations, a statistical survey of 880 petroglyph-bearing rock surfaces within the conservation area of the Damaidi petroglyph site was first conducted to document the orientation of the petroglyph-bearing rock surfaces and the development of blistering and scaling. Subsequently, laboratory experiments were carried out to investigate the differences in P-wave velocity and thermodynamic properties between the black crust and the underlying rock layers (weak interlayer and fresh bedrock). Finally, numerical simulations based on the experimental results were performed to explore the formation mechanisms of blistering and scaling on petroglyph-bearing rock surfaces with black crust under two different temperature variation conditions.

Methods

Petroglyph preservation environment

The Damaidi petroglyph is located in Zhongwei City, Ningxia Hui Autonomous Region. The precise geographical location is shown in Fig. 1 (105.18°E, 37.51°N). The Damaidi petroglyph area spans approximately 2.51 km east-west and 1.27 km north-south, covering a total area of about 2.97 km². A total of 880 petroglyphs are distributed throughout the region, with each engraved rock surface counted as a single petroglyph. The area is characterized by multiple east-west-trending and nearly parallel ridges, with petroglyphs primarily carved onto the exposed rocks on the ridges. The bedrock of the petroglyph is medium- to fine-grained feldspathic sandstone.

According to data from the Ningxia Meteorological Bureau, the annual average temperature and rainfall in the Damaidi region over the past five years (2020–2024) are shown in Fig. 2³⁶. The average annual temperature over the past five years was 9.45 °C, while the mean annual rainfall was 183.02 mm. More than 70% of the total annual rainfall occurred between June and September. During months when the average temperature in the study area fell below zero, rainfall was relatively low. Notably, the months with the highest temperatures generally coincided with those experiencing the greatest rainfall. Such simultaneous high temperatures and substantial rainfall can result in significant temperature fluctuations at the rock surface.

Deterioration phenomena

To ensure consistent terminology for surface deterioration of petroglyph-bearing rock at the Damaidi site, this study adopts the descriptions provided in the “Illustrated glossary on stone deterioration patterns” published by the International Council on Monuments and Sites (ICOMOS). Based on the descriptions in the glossary, this paper investigates the deterioration phenomena of “blistering” and “scaling”. Blistering refers to the phenomenon in which a slab-like rock layer of a certain thickness on the rock surface undergoes uplift deformation and locally detaches from the underlying substrate, resulting in the formation of cavities behind the slab. It is considered an intermediate stage of scaling. In the study by Collins et al.^{33,34}, Lamp et al.³⁵, and Wei et al.³⁷, this phenomenon is also referred to as “detachment” and “hollowing”. Delamination refers to the process by which thin slabs of rock—typically ranging from millimeters to centimetres in thickness—detach from the surface of a rock mass under relatively low external stress. This form of detachment generally develops parallel to the rock surface. In the study by Collins et al.^{33,34} and Lamp et al.³⁵, this phenomenon is also referred to as “exfoliation”, “spalling” and “flaking”. The field images corresponding to each deterioration term are displayed in Fig. 3. The schematic diagram of the surface structure of the petroglyph-bearing rock is shown in Fig. 4.

In situ tests

To monitor the temperature variations on the surface and at different depths of the petroglyph-bearing rock, temperature sensors were used to measure the temperature at both the surface and various depths. The monitoring was conducted using the TH40W-EX wireless temperature monitor (Chinese). The wireless temperature monitor is powered by batteries or solar energy, with a monitoring range of –30 °C to 65 °C, a resolution of 0.1 °C, and an accuracy of ±0.3 °C. The monitoring process is shown in Fig. 5. First, the temperature sensors are fixed onto the cable at predetermined intervals. Then, a sun-facing rock with a 180° orientation is selected on site using a compass. After drilling to the designed depth and diameter, the cable with the sensors is lowered into the hole. The rock debris generated by drilling is then backfilled to ensure good thermal contact between the sensors and the rock. The monitoring depths are 1, 3, 5, 7, 9, 15, 20, and 30 cm. The monitoring period lasted from August 2023 to April 2024, with data recorded at 30-min intervals. The monitoring data were uploaded to the cloud monitoring platform via 4 G network. To enhance the reliability of the monitoring, three monitoring points were set up on site, and the average value of these points was taken as the final result.

As the initial stage of scaling development, blistering is concealed beneath the surface and is not visible to the naked eye. However, the

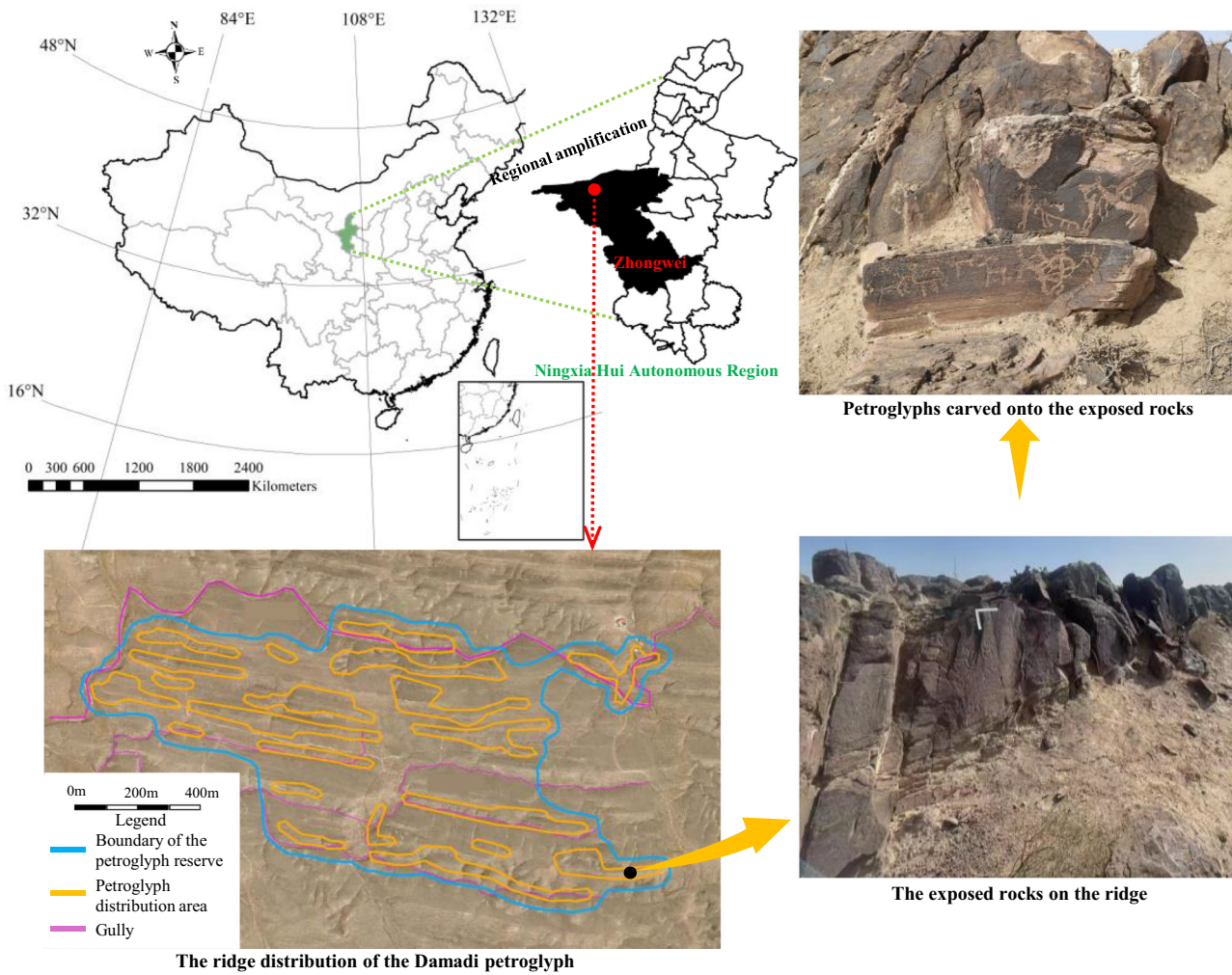
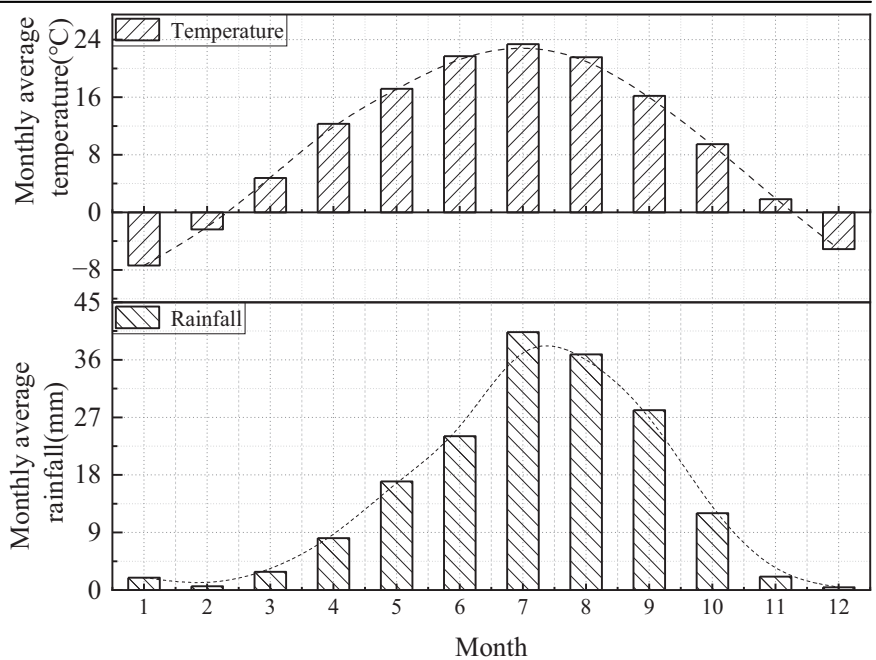
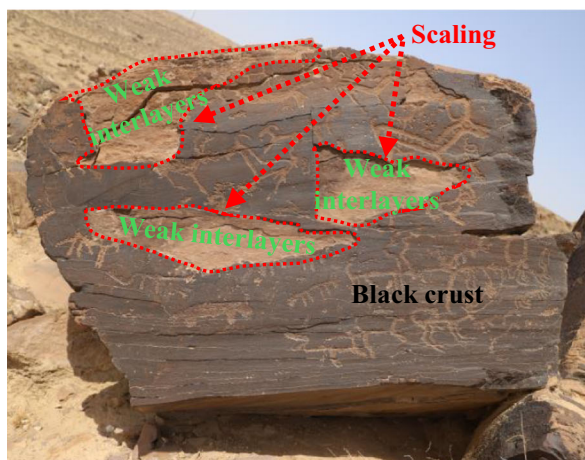


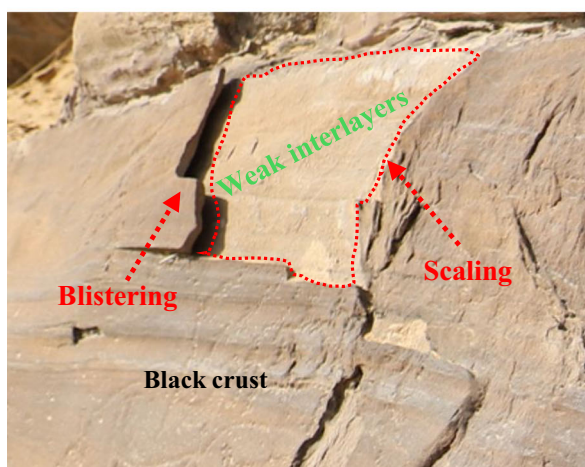
Fig. 1 | Geographical location and distribution of the Damaidi petroglyph. The figure illustrates the geographical location and distribution of the Damaidi petroglyph conservation area, while the right panel presents representative photographs of the Damaidi petroglyphs

Fig. 2 | Climate characteristics of the study area. The figure presents the monthly average temperature and average rainfall in the Damaidi petroglyph site from 2020 to 2024.





(a)



(b)



(c)

Fig. 3 | Scaling and blistering on petroglyph-bearing rock surfaces. **a** Scaling on petroglyph-bearing rock surfaces; **b** Blistering on petroglyph-bearing rock; **c** Weak interlayer exposed after the black crust scaling. The figure illustrates two types of surface deterioration and the structural characteristics of the petroglyph-bearing rock surface.

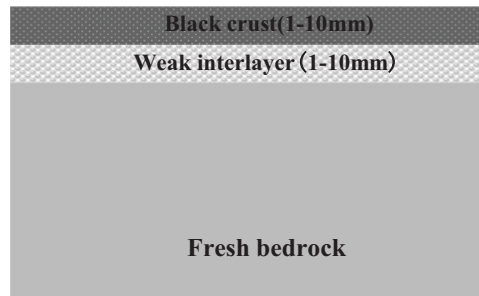


Fig. 4 | Schematic diagram of the surface structure of the petroglyph-bearing rock at the Damaidi. The figure illustrates the structural layers of the petroglyph-bearing rock surface from the exterior to the interior.

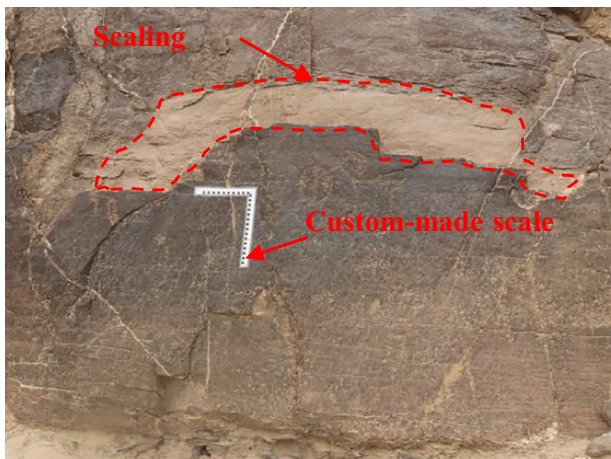
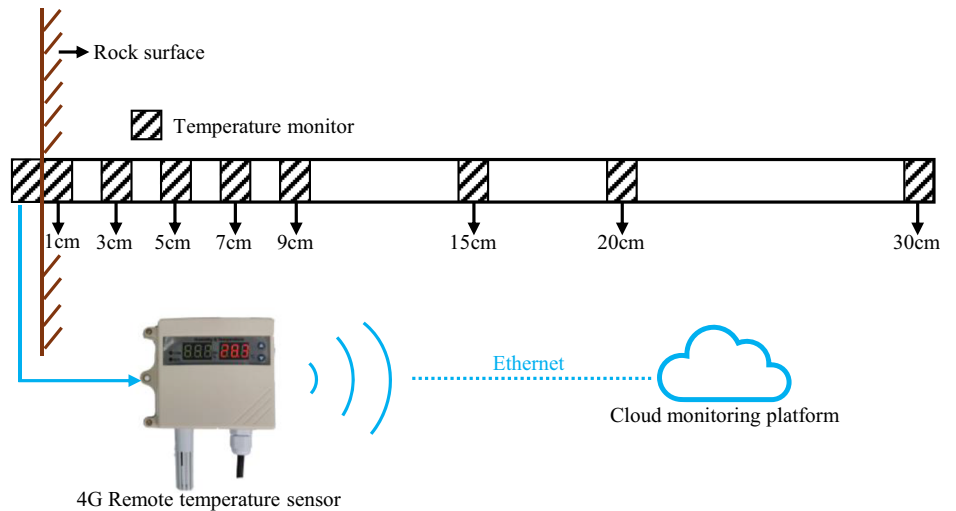
presence of air within blistering causes the surface temperature of the rock above the blistering to differ significantly from that of the surrounding areas. Consequently, thermal infrared imaging technology is currently the primary method for detecting blistering in stone cultural heritage^{38,39}. Rock surfaces with different orientations receive varying durations of solar exposure each day, which reflects differences in the thermal effects experienced by the host rock. To investigate whether the development of surface deterioration on petroglyph-bearing rocks is related to thermal effects, both visible and thermal infrared imaging were conducted for 880 petroglyph-bearing rock surfaces within the study area, and the orientation of the rock surfaces was measured. During imaging, a custom-made scale was affixed to the surface of each petroglyph-bearing rock (Fig. 6) to facilitate subsequent calculation of the areas of scaling and blistering using ImageJ software. Visible light images of the petroglyph-bearing rock surfaces were captured using a Canon 90D high-resolution camera. Thermal infrared images were acquired using the InfraRed Camera R500Pro, manufactured by Nippon Avionics Co. Ltd. (Japan), which operates within a wavelength range of 8–14 μm, a temperature measurement range of –40 to 2000 °C, and a thermal sensitivity of 0.03 °C. The orientation measurements were conducted using a YHL90/360S(A) electronic geological compass manufactured by Harbin Optical Instrument Factory, with a the measurement range of 0–360° and a precision of 0.1°, 0° represents the north.

Laboratory experiments

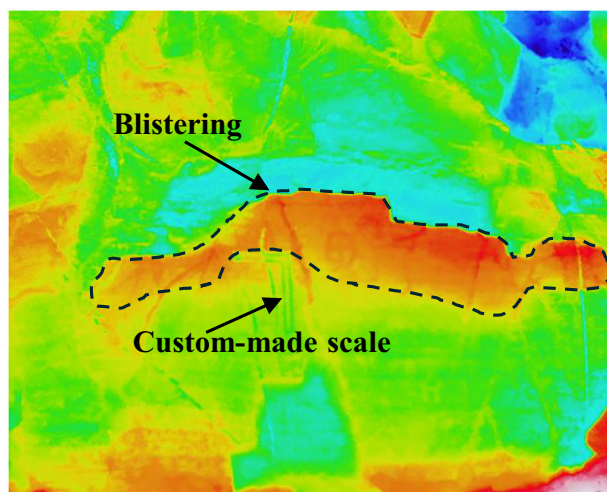
To investigate the differences in P-wave velocity and thermodynamic properties between the black crust and underlying rock layers, in addition to conducting in-situ tests, typical samples of the black crust, weak interlayers exposed after black crust scaling, and fresh bedrock from deeper strata were collected for laboratory analysis (Fig. 7). It is important to emphasize that, in order to avoid damaging the petroglyphs and to ensure that the mineral composition and microstructure of the samples were not affected by nearby soil or vegetation, all rock samples used for laboratory testing were collected from rock surfaces near the petroglyphs but without any carvings. Naturally detached black crust samples were collected, with the requirement that the original location of each black crust on the bedrock could be clearly traced. Additionally, all collected fragments were confirmed to be free from soil coverage and unaffected by surrounding vegetation.

P-wave velocity is a comprehensive indicator reflecting the mechanical properties of rocks as well as the development of porosities and fractures⁴⁰. It offers the advantages of non-destructive testing, making it a commonly used method for evaluating the weathering degree and mechanical performance of stone cultural heritage⁴¹. To investigate differences in P-wave velocity between the black crust on petroglyph-bearing rock surfaces and the underlying rock layers, ultrasonic wave velocity tests were conducted on the black crust and the underlying rock layers. Due to the thinness of the black crust on petroglyph-bearing rock surfaces, conventional non-metallic ultrasonic testing devices are generally inadequate for measuring its P-wave velocity. Therefore, a higher-frequency ultrasonic thickness gauge was employed for this purpose. The ultrasonic thickness gauge determines

Fig. 5 | Temperature monitoring of the petroglyph-bearing rock. The figure presents a flowchart of the temperature monitoring process at the surface and at different depths within the petroglyph-bearing rock.



(a)



(b)

Fig. 6 | Investigation of scaling and blistering on petroglyph-bearing rock surfaces. **a** Visible light images of scaling; **b** Thermal infrared imaging of blistering. The figure illustrates two different methods used to survey these two types of surface deterioration.

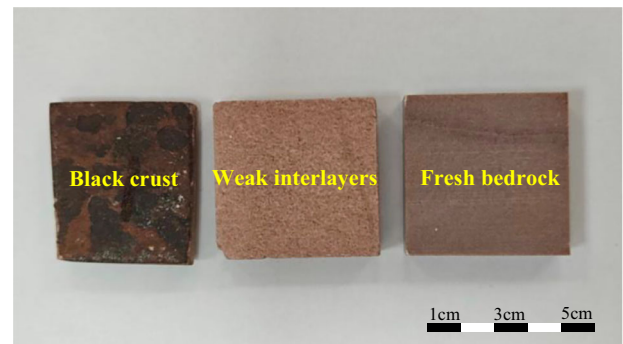


Fig. 7 | Rock samples from different layers of the petroglyph-bearing rock. The figure shows field-collected samples of the surface black crust, the underlying weak interlayer, and the fresh bedrock.

material thickness based on a known P-wave velocity. Conversely, by comparing the actual sample thickness with the measured thickness, the true P-wave velocity can be calculated. In this study, an A1210 ultrasonic thickness gauge manufactured by ACS (Germany) was used. The transducer operates at a frequency of 2.4 MHz, with a velocity range of 500–20,000 m/s, a thickness measurement range of 3–100 mm, and a resolution of 0.1 mm. To improve measurement reliability and account for rock heterogeneity, five samples of each rock layer were tested, and the average value was taken as the representative wave velocity.

To investigate the thermodynamic differences between the black crust on petroglyph-bearing rock surfaces and the underlying rock layers, the black crust, the weak interlayer, and the fresh bedrock were cut into specimens of $50 \times 50 \times 25 \text{ mm}^3$ and $8 \times 8 \times 25 \text{ mm}^3$ for testing the thermal conductivity and thermal expansion coefficient, respectively. Thermal conductivity was measured using the HotDisk 2500S thermal constants analyzer (Sweden), with a measurement range of 0.005–500 W/m·K, a test temperature of 25 °C, and an accuracy of $\pm 3\%$. The thermal expansion coefficient was measured using the DIL 402 C/4/G dilatometer (Germany), operating at a heating rate of 5 K/min, with a measurement range of $\pm 5000 \mu\text{m}$ and a displacement resolution of 0.125 nm. For each rock layer, five samples were tested, and the average value was used as the representative result.

Numerical simulation

As a numerical simulation software for geotechnical engineering, FLAC3D is based on the explicit Lagrangian finite difference method, which makes it easier to achieve convergence in large deformation simulations compared

with general-purpose software. To investigate the influence of the properties differences between the black crust and the underlying rock layers on the blistering and scaling of the petroglyph-bearing rock under thermal effects, a numerical model of the petroglyph-bearing rock, the black crust and the underlying rock layers at the Damaidi site was constructed using FLAC3D. Based on field monitoring of temperature on the rock surface and at different internal depths, the model simulates the distribution of temperature, strain, and stress within the rock body under thermal loading. For comparison, we also constructed a control model of the fresh bedrock and the black crust, without a weak interlayer.

Based on the temperature monitoring results at different depths within the rock (Fig. 14), it was determined that the primary influence of temperature is confined to the upper 10 cm of the rock. Considering computational efficiency for the numerical simulation, the model dimensions were set to 20 cm in length, 20 cm in width, and 10 cm in depth. Both the black crust and the underlying weak interlayer were assigned a thickness of 1 cm each, as shown in Fig. 8.

Previous studies indicated that the elastic modulus of rock is related to its P-wave velocity, as expressed by Eq. (1)⁴². In this equation, V_p represents the P-wave velocity, ν is Poisson's ratio, typically ranging from 0.2 to 0.3 for sandstone, with a value of 0.25 adopted in this study, and ρ is the rock density, which can be determined using the water displacement method. Consequently, the elastic moduli of the black crust, underlying weak interlayer, and fresh bedrock were determined from P-wave velocity measurements. Thermodynamic parameters for the three layers were derived from thermodynamic testing (further detailed in Section of *Differences in Thermodynamic Properties between the Black Crust and Underlying Rock Layers*). An isotropic thermal conduction model and elastic constitutive model in FLAC3D were employed, with specific parameters summarized in Table 1. The boundary conditions included normal constraints and adiabatic boundaries on the sides and bottom of the model, with a free boundary on the top surface.

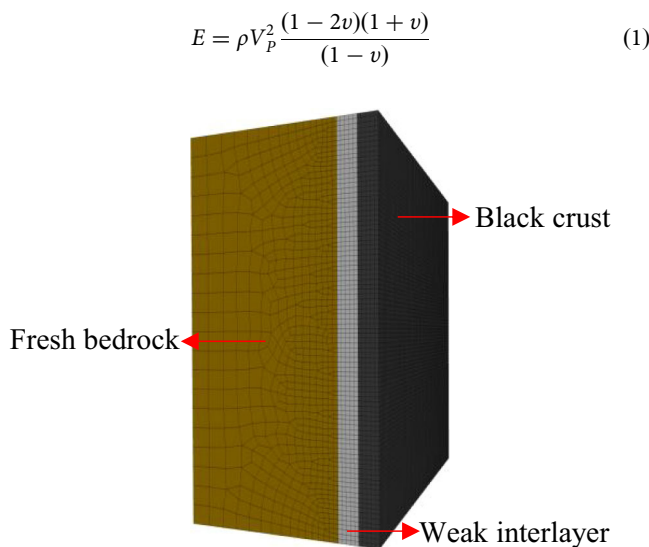


Fig. 8 | Numerical model of petroglyph-bearing rock with black crust. The figure presents a numerical model of the petroglyph-bearing rock surface with a black crust.

Meteorological studies have demonstrated that daily environmental temperature fluctuations can generally be described by a sinusoidal function⁴³, which can be expressed in the general form:

$$T = A * \sin\left(\frac{2\pi}{24} * t + \varphi\right) + C \quad (2)$$

where T represents the temperature at time t , A is the amplitude of the temperature fluctuation, φ is the phase angle, and C is the average temperature.

According to the surface temperature monitoring results of the Damaidi rock (Fig. 13), the daily temperature fluctuations of the rock surface exhibit a sinusoidal pattern similar to that of ambient environmental temperature. However, the surface temperature of the rock is significantly higher than the environmental temperature. Based on the field monitoring, the surface temperature of the rock was set to range from a minimum of 293 K to a maximum of 328 K in the simulation. Due to the long duration of daily temperature cycles, directly applying a 24-h temperature variation would result in excessive computational time. Therefore, in this study, the daily temperature cycle was proportionally shortened, and the period for one complete temperature fluctuation was condensed to 6 h. The corresponding temperature curve is shown in Fig. 9.

Although the Damaidi petroglyphs are located in the transitional zone between semi-desert and desert regions with low annual rainfall, the months with the highest temperatures generally coincide with those receiving the most rainfall. The rate of temperature change in rocks induced by rainfall is significantly higher than that caused by regular daily temperature cycles. Therefore, in addition to long-term exposure to cyclic daily temperature fluctuations, the petroglyph-bearing rock surface at Damaidi is also subject to intermittent abrupt temperature changes. Previous studies have demonstrated that the cooling behavior of general materials follows

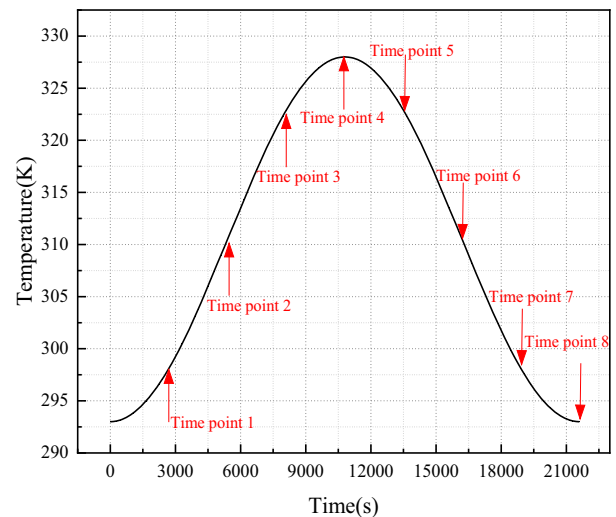


Fig. 9 | Daily temperature fluctuation curve and monitoring points. The figure shows the curve of simplified daily temperature fluctuation and eight monitoring points at different time intervals.

Table 1 | Rock parameters used in the numerical model

| Rock unit | Density (kg/m ³) | Elastic modulus (GPa) | Poisson's ratio | Thermal conductivity W/(m-K) | Specific heat J/(kg-K) | Thermal expansivity |
|-----------------|------------------------------|-----------------------|-----------------|------------------------------|------------------------|---------------------|
| Black crust | 2000 | 20 | 0.25 | 1.73 | 1140 | 9.64 |
| Weak interlayer | 1800 | 6 | 0.25 | 1.12 | 1070 | 6.67 |
| Fresh bedrock | 2500 | 52 | 0.25 | 4.37 | 1150 | 9.96 |

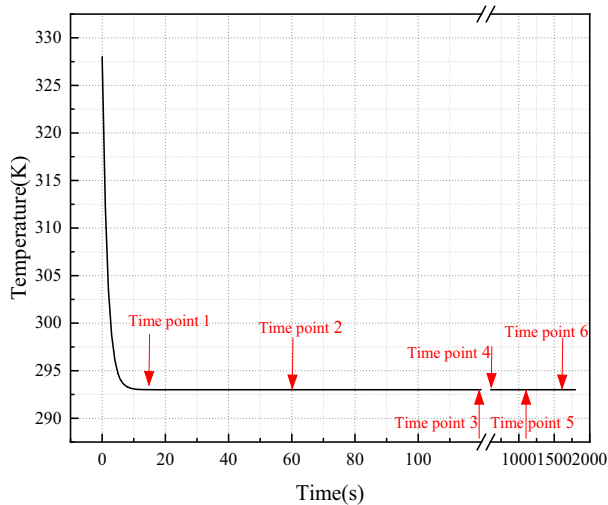


Fig. 10 | Abrupt temperature change curve and monitoring points. The figure shows the variation curve of abrupt temperature change induced by rainfall, along with six monitoring points at different time intervals.

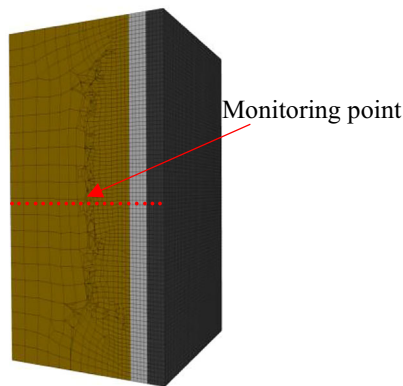


Fig. 11 | Distribution of monitoring points along the rock depth. The figure shows the monitoring points arranged at different depths within the numerical model.

Newton’s Law of Cooling, which describes the exponential decrease of temperature over time. The general form of this law can be expressed as:

$$T = C + (T_0 - C) * e^{-kt} \tag{3}$$

where T is the temperature at time t , T_0 is the initial temperature, k is the decay rate (thermal conductivity), and C represents the environmental temperature.

At standard atmospheric conditions, the thermal conductivity of liquid water is approximately 0.59 W/(m·K), and the typical temperature range of raindrops is between 0 °C and 25 °C⁴⁴. In this study, the raindrop temperature is assumed to be 10 °C. Therefore, to simulate the most unfavorable circumstance, a sudden rainfall event is considered to occur when the rock surface reaches its highest summer temperature. The resulting abrupt temperature change curve is illustrated in Fig. 10.

To quantify the variation in temperature, strain, and stress within the rock during thermal fluctuations, eight monitoring time points were established in the daily temperature fluctuation simulation at intervals of 45 min. These points include the time of peak surface temperature as well as the point when the temperature returns to its initial state, as shown in Fig. 9. In the simulation of abrupt temperature change, the cooling process occurs much faster than the heat conduction within the rock. Therefore, the cooling duration was extended to 30 min. Six monitoring time points were established at 15 s, 1 min, 2 min, 10 min, 20 min, and 30 min, respectively, as shown in Fig. 10. By comparing the temperature, strain increment, and maximum principal stress along the depth of the rock at different time points, this study aims to reveal the mechanical deformation characteristics of rock surfaces covered by the black crust under two distinct temperature loading conditions: daily temperature fluctuation and abrupt temperature change. The spatial arrangement of the depth-direction monitoring points is illustrated in Fig. 11, with all points evenly spaced at 0.5 cm intervals.

Results

Temperature variations on the surface and along the depth of the petroglyph-bearing rock

The temperature variation curves at different depths on the surface and within the petroglyph-bearing rock are shown in Fig. 12. As the temperature in the numerical simulation must be expressed in Kelvin (K), the monitoring results are presented in Kelvin (K) for better comparison and validation.

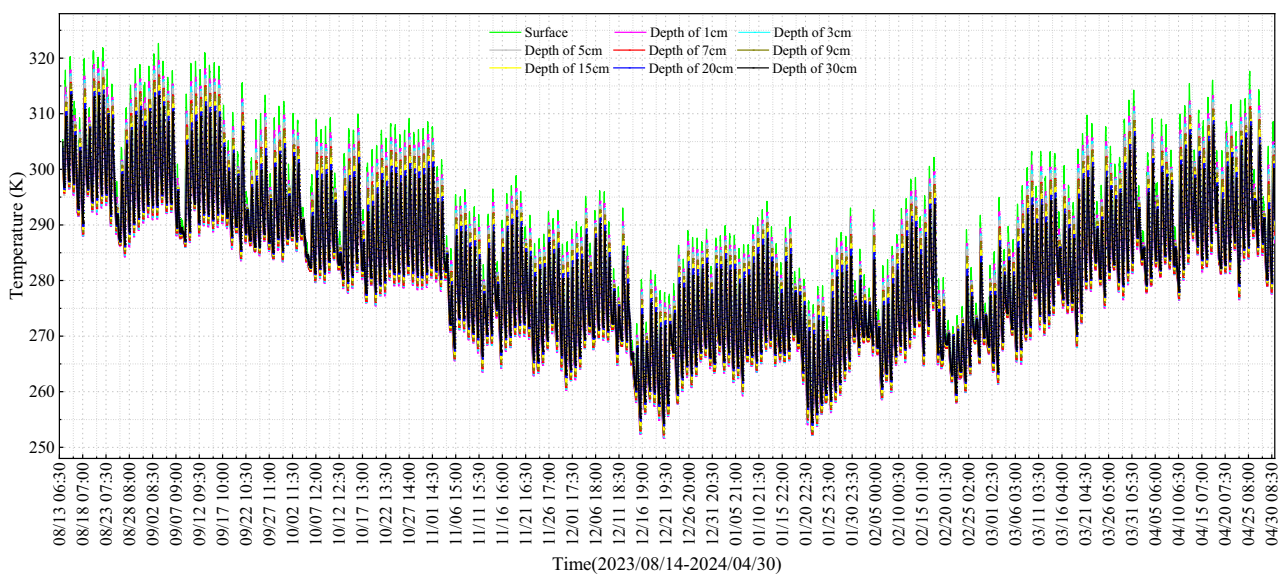


Fig. 12 | The temperature variation curves of the petroglyph-bearing rocks. The figure presents the temperature variation curves measured in situ at the surface and at different depths of the petroglyph-bearing rock.

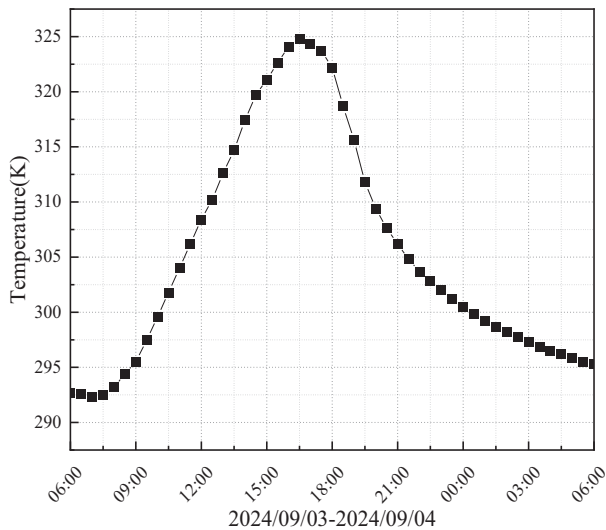


Fig. 13 | Diurnal surface temperature variation of the rock. The figure presents the 24-hour temperature variation curve of the surface of the petroglyph-bearing rock, derived from field monitoring data.

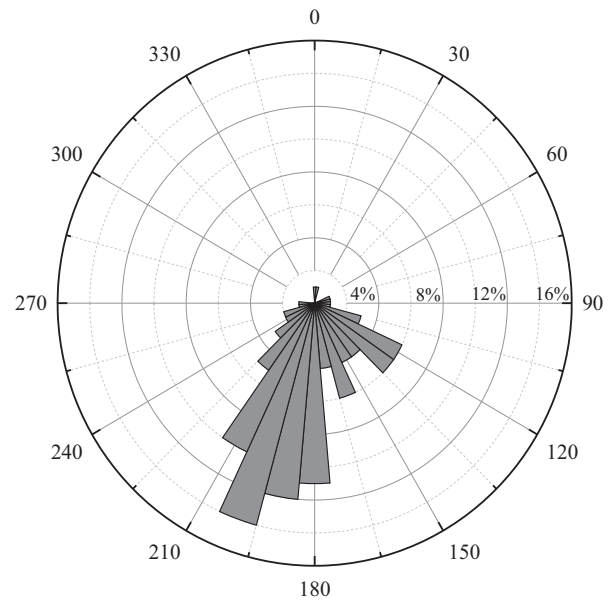


Fig. 15 | Orientation distribution of petroglyph-bearing rock surfaces. The figure shows the distribution range of the orientation of the petroglyph-bearing rock surface measured using a compass.

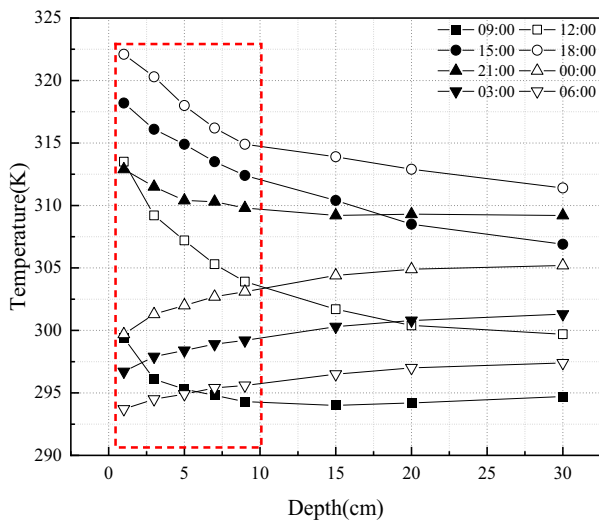


Fig. 14 | Temperature variation along rock depth at different time points of the day. The figure presents the temperature variation curves at different depths of the petroglyph-bearing rock, recorded at 3-hour intervals based on field monitoring data.

During the monitoring period, the highest recorded surface temperature occurred on September 3, reaching 325 °C. A detailed 24-h temperature profile from 06:00 am on September 3 to 06:00 am on September 4 was plotted, as shown in Fig. 13. As illustrated, the surface temperature rose and then declined over the 24-h period, exhibiting a pattern resembling a sinusoidal function.

To further analyze vertical thermal responses, the 24-h period from 06:00 on September 3 to 06:00 on September 4 was divided into eight evenly spaced time points, and temperature profiles along the rock depth were plotted for each time point (Fig. 14). Steeper temperature gradients were observed closer to the surface. Additionally, the rate of temperature change within the rock differs notably within two distinct depth intervals: when the depth is less than 10 cm, the temperature gradient is relatively steep; beyond 10 cm, the gradient significantly reduced. This indicates that the primary influence of temperature fluctuations is confined to the upper 10 cm of the rock, and thermal effects on deeper layers are significantly weaker.

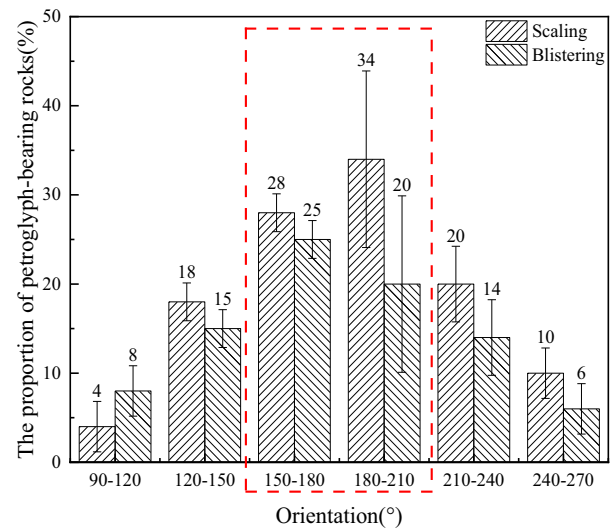


Fig. 16 | Relationship between the development of blistering and scaling on the surface of the petroglyph-bearing rock and orientation. The figure shows the proportion of petroglyph-bearing rocks with blistering and scaling under different orientation ranges.

Relationship between the development of blistering and scaling and the orientation of petroglyph-bearing rocks

Based on the orientation measurements of 880 petroglyph-bearing rock surfaces within the study area, the resulting orientation rose diagram is presented in Fig. 15. The orientations of petroglyph-bearing rocks are predominantly distributed between 90° and 270° (95%), with a concentration between 180° and 210° (37%), 0° represents the north.

To investigate the relationship between blistering and scaling and the orientation of petroglyph-bearing rock surfaces, the orientation range of 90°–270° was evenly divided into six angular intervals. The proportion of petroglyph-bearing rocks exhibiting blistering and scaling features within each orientation interval was statistically analyzed, as shown in Fig. 16. The

proportion of petroglyph-bearing rocks with blistering and scaling first increases and then decreases with increasing orientation angles, with a peak occurring in the range of 150°–210°. These findings suggest that blistering and scaling are more susceptible to developing when the petroglyph-bearing rock orientation approaches approximately 180°.

Because Damaidi petroglyphs are located in the Northern Hemisphere, rock surfaces oriented between 150° and 210° receive sunlight for longer durations within a day compared to those oriented between 90°–150° and 210°–270° (Fig. 17). This results in more intense thermal effects. Consistent with this, Collins et al.³⁵ showed that crack propagation and rockfall are more likely to occur during the warmest times of the day and year based on

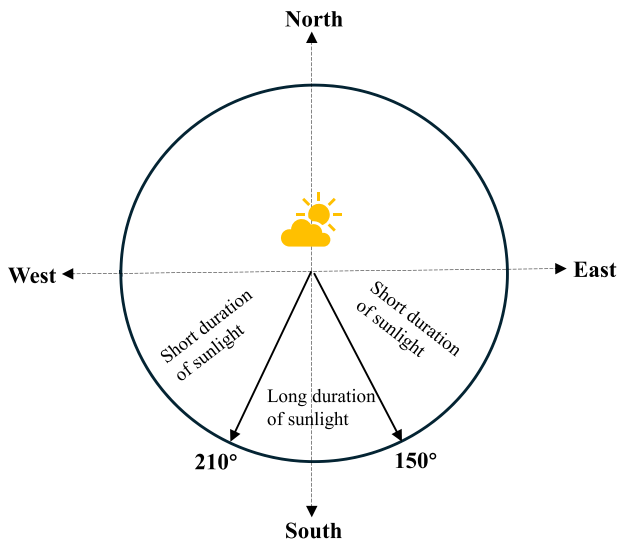


Fig. 17 | Schematic diagrams of the relationship between rock surface orientation and duration of sunshine. The figure shows the relationship between different orientations of the petroglyph-bearing rock surface and the duration of sunshine.

Table 2 | P-wave velocities of the black crust, weak interlayer, and fresh bedrock samples

| Sample number | P-wave velocity of the black crust (m/s) | P-wave velocity of the weak interlayer (m/s) | P-wave velocity of the fresh bedrock (m/s) |
|---------------|--|--|--|
| 1 | 3125 | 1907 | 4110 |
| 2 | 2778 | 1913 | 3797 |
| 3 | 3289 | 2023 | 3896 |
| 4 | 2795 | 2083 | 4615 |
| 5 | 2851 | 1976 | 4348 |
| Average | 2967.6 | 1980.4 | 4153.2 |

field monitoring. The above analysis indicates that the blistering and scaling on the petroglyph-bearing rock surface are related to temperature effects.

Differences in P-wave velocity between the black crust and underlying rock layers

The P-wave velocities of the black crust, weak interlayer, and fresh bedrock samples measured by the ultrasonic thickness gauge are presented in Table 2. The average P-wave velocity of the weak interlayer samples is 1980.4 m/s, that of the black crust is 2967.6 m/s, and that of the fresh bedrock is 4153.2 m/s. These results indicate that the fresh bedrock exhibits the highest P-wave velocity, while the weak interlayer shows the lowest, approximately 47.7% of that of the fresh bedrock. The black crust’s average P-wave velocity lies between the two, approximately 1.5 times higher than the weak interlayer and 71.5% of the fresh bedrock velocity.

Differences in thermodynamic properties between the black crust and underlying rock layers

The measured thermal conductivity and thermal expansion coefficients of the black crust, weak interlayer, and fresh bedrock samples are presented in Table 3. The average thermal conductivity values for the fresh bedrock, weak interlayer, and black crust are 4.37, 1.12, and 1.73 W/m·K, respectively. The corresponding average thermal expansion coefficients are $9.96 \times 10^{-6}/K$, $6.67 \times 10^{-6}/K$, and $9.64 \times 10^{-6}/K$. These results indicate that the fresh bedrock exhibits the highest thermal conductivity and thermal expansion coefficient, while the weak interlayer shows the lowest values (25.6% and 66.9% of fresh bedrock, respectively). The black crust falls in between (1.5 and 1.4 times those of the weak interlayer, and 39.6% and 96.7% of fresh bedrock, respectively).

Influence of the black crust on the development of blistering and scaling under thermal effects

The temperature distribution cloud maps in the model of the petroglyph-bearing rock under both daily temperature fluctuation and abrupt temperature change conditions are shown in Fig. 18. Due to space limitations, only one time point is presented here. Based on the numerical simulation results, temperature values were extracted from the vertical monitoring points, and the temperature variation curves along the rock depth at different time points were plotted, as shown in Fig. 19.

(1) In Fig. 19a, under daily temperature fluctuation, the rock surface in the model exhibits higher temperatures than the interior prior to time point 5, with temperature gradually decreasing with depth. After time point 6, the surface temperature drops below that of the interior, and temperature increases progressively with depth. This indicates a noticeable lag in sub-surface temperature response relative to surface temperature changes.

(2) In Fig. 19b, under abrupt temperature change, the surface temperature in the model of the rock decreases rapidly over time, resulting in lower surface temperatures compared to the interior.

(3) Fig. 19 also reveals that the temperature gradient is steeper closer to the rock surface under both daily temperature fluctuation and abrupt temperature change. Notably, compared with the model without a weak

Table 3 | Thermal conductivity and thermal expansion coefficients of the black crust, weak interlayer, and fresh bedrock

| Sample number | Black crust | | Weak interlayer | | Fresh bedrock | |
|---------------|-----------------------------|------------------------------|-----------------------------|------------------------------|-----------------------------|------------------------------|
| | Thermal conductivity (W/mK) | Thermal expansivity (*E-6/K) | Thermal conductivity (W/mK) | Thermal expansivity (*E-6/K) | Thermal conductivity (W/mK) | Thermal expansivity (*E-6/K) |
| 1 | 1.74 | 8.59 | 1.12 | 5.79 | 4.31 | 10.04 |
| 2 | 1.79 | 10.92 | 1.13 | 5.44 | 4.43 | 9.69 |
| 3 | 1.65 | 9.40 | 1.11 | 5.72 | 4.31 | 9.58 |
| 4 | 1.75 | 10.11 | 1.10 | 7.62 | 4.51 | 9.93 |
| 5 | 1.70 | 9.18 | 1.14 | 8.79 | 4.29 | 10.56 |
| Average | 1.73 | 9.64 | 1.12 | 6.67 | 4.37 | 9.96 |

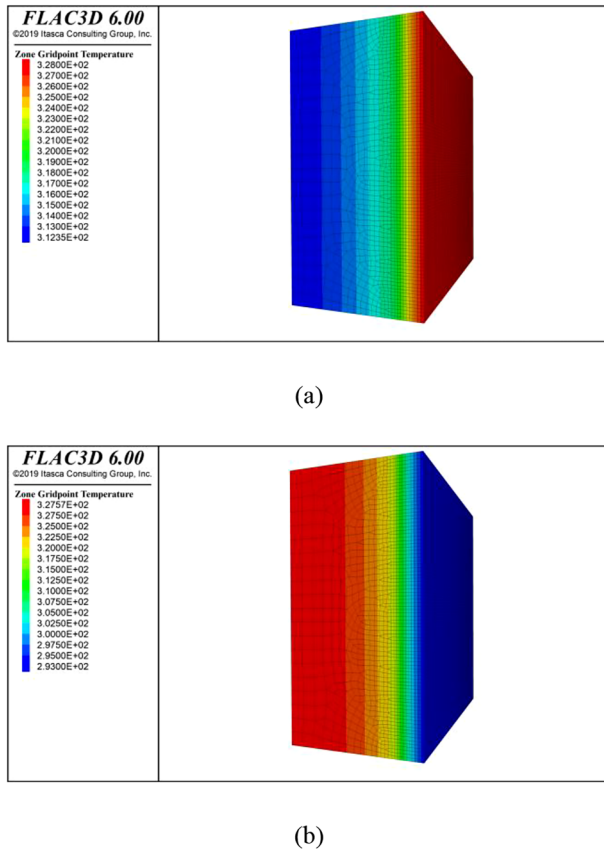


Fig. 18 | Temperature distribution of the petroglyph-bearing rock under two temperature conditions. a Daily temperature fluctuation at time point 4; **b** Abrupt temperature change at time point 4. The figure presents temperature cloud maps of the petroglyph-bearing rock at a specific moment under daily temperature fluctuations and abrupt temperature changes.

interlayer, the model incorporating a weak interlayer exhibits a more pronounced nonlinear gradient transition within the depth range of 0.5–2.0 cm. The highest rate of temperature change occurs within the black crust near the rock surface, but drops markedly upon reaching the underlying weak interlayer with lower thermal conductivity, highlighting the thermal discontinuity between the two layers.

A comparison between the numerical simulation and field monitoring results (Figs. 14 and 19) of rock temperature variations with depth at the same time indicates that the two exhibit generally consistent trends, although slight numerical differences are present. Both results show that the temperature gradient becomes increasingly pronounced closer to the rock surface. Because the temperature variation curve used in the numerical simulation takes into account the temperature changes in the study area over the years, slight numerical differences from the field measurements are expected. A comparison of the numerical simulation and field monitoring results for rock temperature variations with depth at different times shows that, similar to the field monitoring, the numerical simulation also indicates a noticeable lag in the internal rock temperature response relative to surface temperature changes. This pattern is similar to the temperature variations observed at different depths of rock at a petroglyph site in South Africa monitored by Stéphane Hoerlé between 15 June and 31 July 2004²⁵. These results indicate that the numerical simulation method employed is reliable for investigating the thermal stress distribution within the petroglyph-bearing rocks at the Damaidi.

The maximum principal stress reflects the internal stress state of the material and can be used to evaluate the stress differences between the black crust and the underlying rock layers. A greater difference in maximum

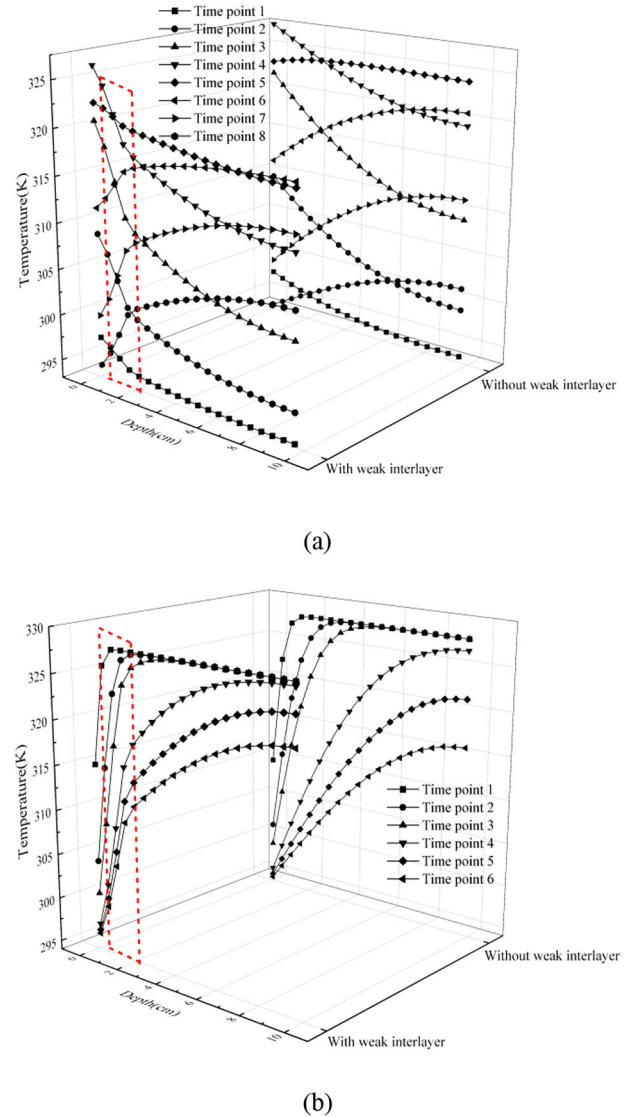
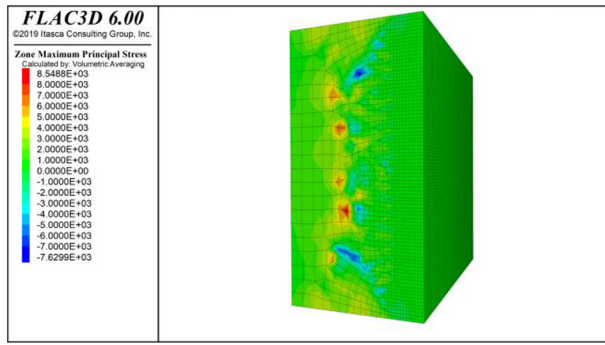


Fig. 19 | Temperature variation curves along the depth of the petroglyph-bearing rock at different time points under two temperature conditions. a Daily temperature fluctuations; **b** Abrupt temperature changes. The figure presents the temperature profiles along the depth of the petroglyph-bearing rock at different times under daily temperature fluctuations and abrupt temperature changes.

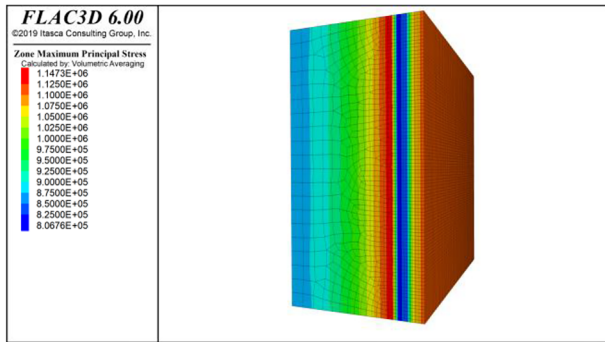
principal stress indicates a more pronounced mechanical mismatch between the two layers. The cloud maps of maximum principal stress in the model of petroglyph-bearing rock under daily temperature fluctuation and abrupt temperature change are shown in Fig. 20. Due to space limitations, only one point in time is displayed. Based on the numerical simulation results, the maximum principal stress values were extracted from the vertical monitoring points, and the stress variation curves along the rock depth at different time points were plotted, as shown in Fig. 21.

(1) In Figs. 20a and 21a, under daily temperature fluctuation, the maximum principal stress values at different time points remain relatively low. Additionally, there is no significant depth-dependent change in maximum principal stress. Minor fluctuations in the curves are attributed to local mesh distortions in the numerical model. These results indicate that daily temperature fluctuation does not induce notable stress concentration within the model of the rock body.

(2) In Figs. 20b and 21b, the maximum principal stress in the rock under abrupt temperature change is significantly higher than that under daily temperature fluctuation. During abrupt cooling, the maximum



(a)



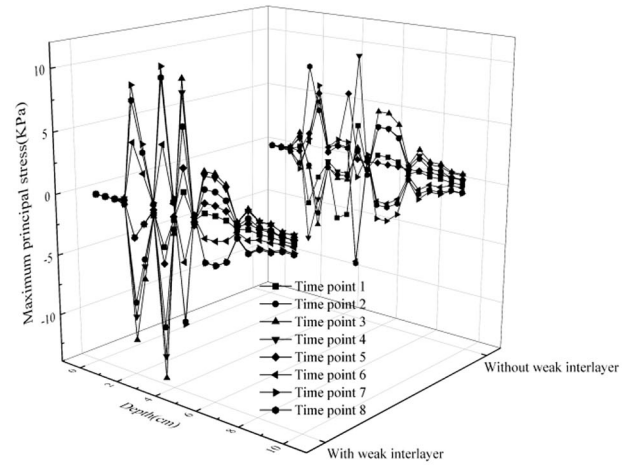
(b)

Fig. 20 | Cloud maps of maximum principal stress in the rock under two temperature conditions. a Daily temperature fluctuation at time point 5; **b** Abrupt temperature change at time point 5. The figure presents cloud maps of the maximum principal stress within the petroglyph-bearing rock at a specific moment under daily temperature fluctuation and abrupt temperature change.

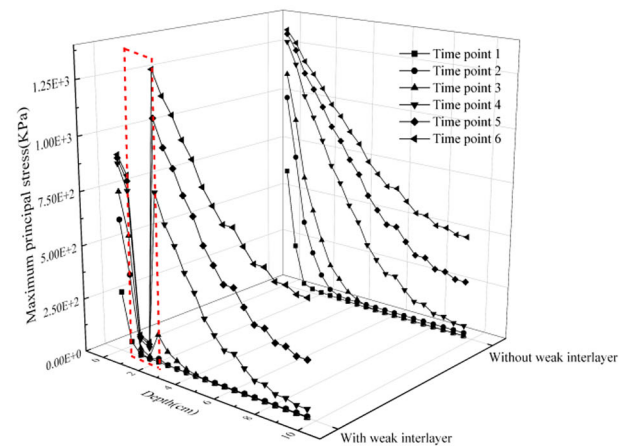
principal stress increases progressively over time. When a weak interlayer is present, the zones of maximum principal stress are concentrated near the surface of the model prior to time point 4. After time point 4, the zones of maximum stress shift to the interior of the rock. In contrast, in the absence of a weak interlayer, the maximum principal stress is always greatest at the rock surface. These results suggest that abrupt temperature change induces the formation of stress concentration zones within rock models containing a weak interlayer.

(3) In Fig. 21, unlike the relatively smooth trend observed under daily temperature fluctuation, the model incorporating a weak interlayer exhibits a sudden drop followed by a sharp rise in the maximum principal stress within the depth range of 0.5–2.0 cm under abrupt temperature change. This jump-like behavior indicates the presence of discontinuous stress gradients at the interface between the weak interlayer and its adjacent layers (the outer black crust and the inner fresh bedrock). These results suggest that, under abrupt temperature changes, the existence of the weak interlayer facilitates the development of stress discontinuities at this interface, making the rock surface more prone to separation and the formation of blistering or scaling.

The strain increment reflects the deformation state of the material and can reveal differences in deformation between the black crust and the underlying rock layers. A larger difference in strain increment indicates a greater degree of non-uniform deformation. The cloud maps of strain increment under daily temperature fluctuation and abrupt temperature change are shown in Fig. 22. Due to space limitations, only one time point is displayed. Based on the numerical simulation results, the strain increment values were extracted from the vertical monitoring points, and the strain



(a)



(b)

Fig. 21 | Variation curves of maximum principal stress along the depth of the petroglyph-bearing rock at different time points under two temperature conditions. a Daily temperature fluctuations; **b** Abrupt temperature changes. The figure presents the variation curves of maximum principal stress along the depth of the petroglyph-bearing rock at different times under daily temperature fluctuations and abrupt temperature changes.

increment variation curves along the rock depth at different time points were plotted, as shown in Fig. 23.

(1) In Fig. 23a, under daily temperature fluctuation, the strain increment at the rock surface initially increases and subsequently decreases, reaching a peak at time point 4. Except for the depth range of 0.5–2.0 cm, the strain increment decreases gradually with depth before time point 5. After time point 6, the strain increment gradually increases with depth. This indicates that the strain increment response within the rock exhibits a noticeable lag relative to surface temperature variations.

(2) In Fig. 23b, under an abrupt temperature change, the absolute values of strain increment gradually increase over time. Except within the depth range of 0.5–2.0 cm, the strain increment generally decreases with increasing depth. Furthermore, strain increments exhibit higher rates of change closer to the surface.

(3) In Fig. 23, under both daily temperature fluctuation and abrupt temperature change, the model incorporating a weak interlayer exhibits a sudden decrease followed by an abrupt increase in the absolute values of strain increments within the depth range of 0.5–2.0 cm, compared with the

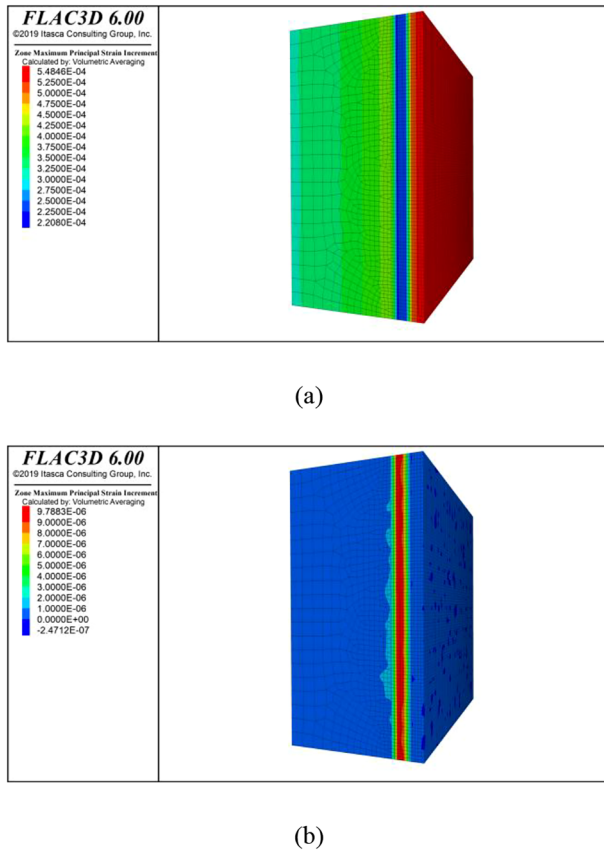


Fig. 22 | Cloud maps of strain increment in the rock under two temperature conditions. **a** Daily temperature fluctuation at time point 4; **b** Abrupt temperature change at time point 1. The figure presents cloud maps of the strain increment within the petroglyph-bearing rock at a specific moment under daily temperature fluctuation and abrupt temperature change.

model without a weak interlayer. This indicates a discontinuous gradient deformation at the interfaces between the weak interlayer and its adjacent layers. Consequently, the presence of the weak interlayer facilitates the separation of the rock surface and promotes the formation of blistering and scaling.

Although the model with a weak interlayer exhibits jump-like variations in strain increments within the 0.5–2.0 cm depth range under both temperature loading conditions, the increments are positive under daily temperature fluctuation and negative under abrupt temperature change. This finding suggests that, under daily temperature fluctuation, the initial separation typically occurs at the interface between the black crust and the underlying weak interlayer, causing scaling predominantly of the black crust. In contrast, under abrupt temperature change, the separation typically initiates at the interface between the weak interlayer and the fresh bedrock below, resulting in scaling involving not only the black crust but also portions of the weak interlayer.

Discussion

Previous studies have shown that the threshold value for temperature change rates inducing thermal shock damage in rock is approximately 2 °C/min. When the rate of temperature change is below this threshold, rock damage primarily occurs through thermal fatigue. However, when the temperature change rate equals or exceeds this threshold, the rock attempts to adjust at a rate exceeding its plastic deformation capability, resulting in irreversible plastic strain and structural damage^{45,46}. At the Damaidi petroglyph site, the petroglyph-bearing rocks experience their most rapid daily temperature changes during morning warming (time point 2) and

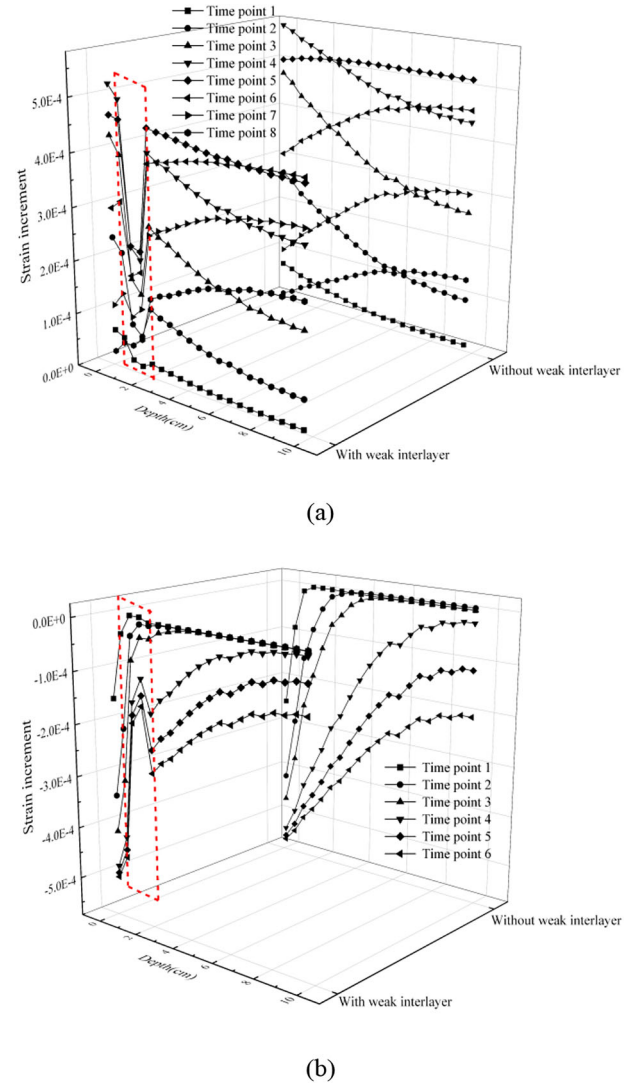


Fig. 23 | Variation curves of strain increment along the depth of the petroglyph-bearing rock at different time points under two temperature conditions. **a** Daily temperature fluctuations; **b** Abrupt temperature changes. The figure presents the variation curves of strain increment along the depth of the petroglyph-bearing rock at different times under daily temperature fluctuations and abrupt temperature changes.

afternoon cooling (time point 6). The rate of temperature change during these periods is $\Delta T/t = 0.07$ °C/min, which is significantly below the thermal shock threshold. In contrast, the instantaneous temperature change rate ($\Delta T/t = 35$ °C/min) caused by rainfall-induced abrupt cooling substantially exceeds the thermal shock threshold. This explains why numerical simulations revealed the maximum principal stress within the rock remains low without clear stress concentration zones under daily temperature fluctuations, but significant stress concentrations with considerably higher maximum principal stresses under abrupt temperature changes (Fig. 21). As described by Walker, cracking sounds are often heard from rocks after such storms in hot desert environments⁴⁷. Moreover, Eppes et al.³¹ found through acoustic emission and temperature monitoring of rocks under insolation that most cracking occurs when storms or other weather events strongly perturb the rock surface temperature field at these times, further supporting this conclusion.

Meanwhile, the differences in thermodynamic properties (thermal conductivity and thermal expansion coefficient) between the black crust and the underlying rock layers result in varying thermal expansion and

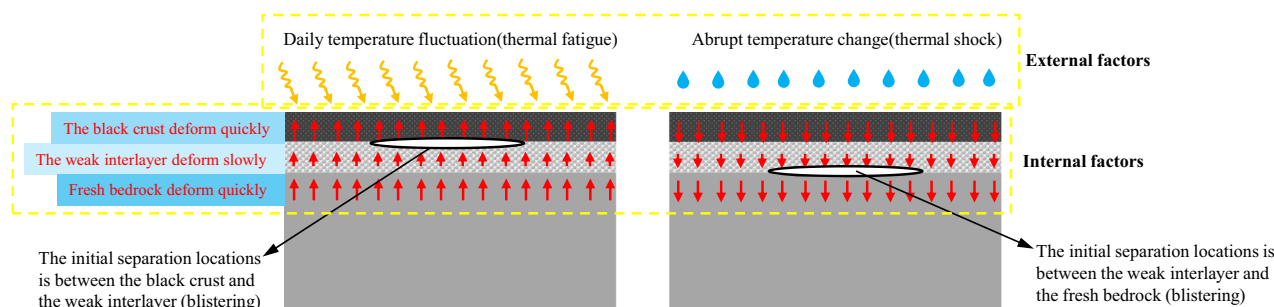


Fig. 24 | Schematic diagram of the initial separation process of the petroglyph-bearing rock surface under two thermal conditions. The figure illustrates the causes and locations of separation within the petroglyph-bearing rock surface under daily temperature fluctuations and abrupt temperature changes.

contraction responses under temperature fluctuations. Additionally, the mechanical strength of the weak interlayer sandwiched between the black crust and fresh bedrock is significantly lower. This creates a distinct “hard-soft-hard” structural configuration that undermines the integrity of the rock surface. Consequently, thermal stresses preferentially damage the weaker internal weak interlayer rather than the harder outer black crust, as confirmed by field observations of blistering and scaling features (Fig. 3).

In summary, the formation of blistering and scaling on petroglyph-bearing rock surfaces is driven by both external and internal factors. Externally, the harsh climatic conditions at the petroglyph site subject the rock surface to long-term thermal fatigue and intermittent thermal shock. Internally, the primary cause is the differences in thermodynamic and mechanical properties between the weak interlayer and the adjacent black crust above and the fresh bedrock below. Under conditions of thermal fatigue from daily temperature fluctuations and thermal shock from abrupt temperature changes, nonlinear gradient deformation and stress concentration develop within the weak interlayer (Figs. 21 and 23). Consequently, separation occurs at the weak interlayer interface between the black crust and the fresh bedrock, leading to the formation of blistering or scaling. Since a single cycle of daily temperature fluctuation induces low internal stress within the rock, abrupt temperature changes are more likely to trigger interlayer separation, leading to the formation of blistering or scaling. Nonetheless, strain increment cloud maps indicate that daily temperature fluctuations also produce discontinuous gradient deformation at the interfaces between the weak interlayer, black crust, and fresh bedrock (Fig. 23). Moreover, Eppes et al.³² demonstrated that thermal stresses associated with temperature change rates of less than $0.2\text{ }^{\circ}\text{C min}^{-1}$ are also to induce subcritical crack propagation through continuous monitoring of acoustic emissions and temperature in sun-exposed granite boulders. Similarly, Collins et al.³³ noted that cyclic thermal forcing may enhance the efficacy of other, more typical exfoliation triggers, thereby making rocks more susceptible to cracking triggered by added stress from other weathering mechanisms. Therefore, the impact of thermal fatigue from daily temperature fluctuations on the development of blistering and scaling should not be disregarded. Furthermore, strain increment analyses reveal differences in the initial separation locations of blistering and scaling under daily temperature fluctuations compared to abrupt temperature changes. A schematic representation of these initial separation processes under both temperature conditions is illustrated in Fig. 24. Based on the formation mechanisms of the blistering and scaling on the petroglyph-bearing rock surface, it is recommended that, in future petroglyph conservation efforts, the direct impact of solar radiation and rainwater on the petroglyph-bearing rock should be minimized as much as possible. This can be achieved by installing sun shields in areas with concentrated petroglyphs.

This study focuses on the formation mechanisms of blistering and scaling on the petroglyph-bearing rock surfaces with black crust and weak interlayer structures under temperature effects. However, our findings are also applicable to exfoliation issues in rocks with similar surface structures

and climatic conditions^{17,18}. Furthermore, based on the results of this study, it can be concluded that it is the presence of the weak interlayer that causes cracks parallel to the rock surface to first form at a certain depth beneath the surface under thermal effects. These cracks then progressively expand, ultimately leading to the occurrence of spalling³⁵.

Although the numerical simulation has provided a good explanation for the formation mechanisms of blistering and scaling on the petroglyph-bearing rock surface under thermal effects, it still has some limitations. Firstly, our model assumes a planar rock surface and does not take into account how a more complex, irregular surface may influence thermal stresses. For example, Martel et al.^{48,49} and Stock et al.⁵⁰ showed that surface curvature can exacerbate surface-normal tensile stresses. Secondly, this study primarily investigates how differences in the physical properties between the black crust and the underlying weak interlayer on the petroglyph-bearing rock influence surface deterioration. It does not explicitly account for the intrinsic heterogeneity within each rock layer. Accordingly, our resulting thermal stresses are calculated assuming a homogenous rock and do not take into consideration the effects of grain-scale processes and the influence of the mismatch in thermal and mechanical properties^{51–54}. Including these effects would likely increase the maximum thermal stresses at the rock surface, thereby facilitating subcritical crack propagation. Moreover, Nara⁵⁵ investigated subcritical crack growth parameters under various environmental conditions and found that these parameters are influenced by factors such as the temperature, humidity and existence of water. Therefore, these influencing factors should be taken into account in future studies.

Data availability

All data generated or analyzed during this study are included in this article. The raw data are available from the corresponding author upon reasonable request.

Received: 30 November 2025; Accepted: 9 March 2026;

Published online: 24 March 2026

References

1. Martínez-Pabello, P. U. et al. Lithodiversity and cultural use of desert varnish in the Northern Desert of Mexico. *Bol. Soc. Geol. Mex.* **74**, A100622 (2022).
2. Anati, E. *World Rock Art: The Primordial Language* (Archaeopress, 2010).
3. Khan, M. Rock art of Saudi Arabia. *Arts* **2**, 447–475 (2013).
4. Willcox, A. R. *The Rock Art of Africa* (Taylor and Francis, 2018).
5. McDonald, J. & Veth, P. Rock art in arid landscapes: Pilbara and Western Desert petroglyphs. *Aust. Archaeol.* **77**, 66–81 (2013).
6. Honoré, E. Prehistoric landmarks in contrasted territories: rock art of the Libyan Desert massifs, Egypt. *Quat. Int.* **503**, 264–272 (2019).

7. Rozwadowski, A. Rock art of Northern, Central, and Western Asia. in *Oxford Handbook of the Archaeology and Anthropology of Rock Art*. 151–176 (Oxford University Press, 2017).
8. Groom, K. M., Villa Cervený, N., Allen, C. D., Dorn, R. I. & Theuer, J. Protecting stone heritage in the painted desert: employing the rock art stability index in the Petrified Forest National Park, Arizona. *Heritage*. **2**, 2111–2123 (2019).
9. Neumann, J. T. et al. Artificial weathering of rock types bearing petroglyphs from Murujuga, Western Australia. *Herit. Sci.* **10**, 77 (2022).
10. Zerboni, A. et al. The sustainability of rock art: preservation and research. *Sustainability* **14**, 6305 (2022).
11. Martínez-Pabello, P. U. et al. Rock varnish as a natural canvas for rock art in *La Proveedora*, northwestern Sonoran Desert (Mexico): integrating archaeological and geological evidences. *Quat. Int.* **572**, 74–87 (2021).
12. Parchert, K. J., Spilde, M. N., Porras-Alfaro, A., Nyberg, A. M. & Northup, D. E. Fungal communities associated with rock varnish in Black Canyon, New Mexico: casual inhabitants or essential partners? *Geomicrobiol. J.* **29**, 752–766 (2012).
13. Andreae, M. O. et al. Geochemical studies on rock varnish and petroglyphs in the Owens and Rose Valleys, California. *PLoS ONE* **15**, e0235421 (2020).
14. Black, J. L., MacLeod, I. D. & Smith, B. W. Theoretical effects of industrial emissions on colour change at rock art sites on Burrup Peninsula, Western Australia. *J. Archaeol. Sci. Rep.* **12**, 457–462 (2017).
15. Dietzel, M., Kolmer, H., Pölt, P. & Simic, S. Desert varnish and petroglyphs on sandstone – Geochemical composition and climate changes from Pleistocene to Holocene (Libya). *Geochemistry* **68**, 31–43 (2008).
16. Dorn, R. I. The rock varnish revolution: new insights from microlaminations and the contributions of Tanzhuo Liu. *Geogr. Compass*. **3**, 1804–1823 (2009).
17. Viles, H. A. & Goudie, A. S. Biofilms and case hardening on sandstones from Al-Quwayra, Jordan. *Earth Surf. Process. Landf.* **29**, 1473–1485 (2004).
18. Thomachot, C. & Jeannette, D. Effects of iron black varnish on petrophysical properties of building sandstone. *Environ. Geol.* **47**, 119–131 (2004).
19. Dorn, R. I., Mahaney, W. C. & Krinsley, D. H. Case hardening: turning weathering rinds into protective shells. *Elements*. **13**, 165–169 (2017).
20. Cui, K., Liu, G., Wu, G. & Zhu, P. Study on the characteristics and mechanisms of freeze-thaw damage of rock carrier of Helankou rock paintings under different conditions (in Chinese). *Chin. J. Rock. Mech. Eng.* **38**, 1797–1808 (2019).
21. Wu, G., Cui, K., Ge, C. & Yu, X. The process and mechanisms of freezing and thawing deterioration of petroglyphs under snowmelt and rainfall infiltration. *Coatings* **13**, 543–556 (2023).
22. Kong, X. et al. Experimental study on the degradation of sandstone-petroglyph carriers in Helankou: Effects of freeze-thaw and wet-dry cycles. *iScience*. **27**, 110576 (2024).
23. Lv, R. *Weathering Characteristics and Mechanism Study on the Carrier of Rock Paintings in Helankou* (in Chinese). (Lanzhou University, 2020).
24. Yang, Y. et al. Research on the mechanism of rock painting deterioration in Helan Mountain: a multiple simulation approach (in Chinese). *Chin. J. Arid Land Resour. Environ.* **37**, 124–132 (2023).
25. Hérlié, S. Rock temperatures as an indicator of weathering processes affecting rock art. *Earth Surf. Process. Landf.* **31**, 383–389 (2006).
26. Griggs, D. T. The factor of fatigue in rock exfoliation. *J. Geol.* **44**, 783–796 (1936).
27. Waragai, T. Weathering processes on rock surfaces in the Hunza valley, Karakoram, North Pakistan. *Z. Geomorphol. Suppl.* **119**, 119–136 (1999).
28. Waragai, T. Effects of rock surface temperature on exfoliation, rock varnish, and lichens on a boulder in the Hunza Valley, Karakoram Mountains. Pakistan. *Arct. Alp. Res.* **30**, 184–192 (1998).
29. Hall, K. The role of thermal stress fatigue in the breakdown of rock in cold regions. *Geomorphology* **31**, 47–63 (1999).
30. Hall, K. & André, M.-F. New insights into rock weathering from high-frequency rock temperature data: an Antarctic study of weathering by thermal stress. *Geomorphology* **41**, 23–35 (2001).
31. Eppes, M. C. et al. Deciphering the role of solar-induced thermal stresses in rock weathering. *Geol. Soc. Am. Bull.* **128**, 1315–1338 (2016).
32. Eppes, M. C. et al. Warmer, wetter climates accelerate mechanical weathering in field data, independent of stress-loading. *Geophys. Res. Lett.* **47**, 1–11 (2020).
33. Collins, B. D. & Stock, G. M. Rockfall triggering by cyclic thermal stressing of exfoliation fractures. *Nat. Geosci.* **9**, 395–400 (2016).
34. Collins, B. D. et al. Thermal influences on spontaneous rock dome exfoliation. *Nat. Commun.* **9**, 762 (2018).
35. Lamp, J. L., Marchant, D. R. & Mackay, S. L. Thermal stress weathering and the spalling of Antarctic rocks. *J. Geophys. Res. Earth Surf.* **122**, 3–24 (2017).
36. Hu, D., Liu, C., Wu, C. & Wang, J. Surface crack hazards in arid-region petroglyphs: coupled thermal and freezing effects from northwest China. *Int. J. Archit. Herit.* **1**, 20 (2025).
37. Wei, P., Liu, C., Wang, J., Hu, D. & Wu, C. Study on the parameterized hollow boundary identification method based on infrared thermal imaging. *NDT E Int.* **157**, 103517 (2026).
38. Kordatos, E. Z., Exarchos, D. A., Stavrakos, C., Moropoulou, A. & Matikas, T. E. Infrared thermographic inspection of murals and characterization of degradation in historic monuments. *Constr. Build. Mater.* **48**, 1261–1265 (2013).
39. Lerma, C., Mas, Á., Gil, E., Vercher, J. & Torner, M. E. Quantitative analysis procedure for building materials in historic buildings by applying infrared thermography. *Russ. J. Nondestruct. Test.* **54**, 601–609 (2018).
40. You, M., Su, C. & Li, X. Study on relation between mechanical properties and longitudinal wave velocities for damaged rock samples (in Chinese). *Chin. J. Rock. Mech. Eng.* **27**, 458–467 (2008).
41. Yuan, P., Yang, X. & Zhao, T. Deterioration characteristics of red-bed sandstone acoustic wave properties due to water and salt solution (in Chinese). *Rock. Soil Mech.* **40**, 227–234 (2019).
42. Martínez-Martínez, J., Benavente, D. & García-del-Cura, M. A. Comparison of the static and dynamic elastic modulus in carbonate rocks. *Bull. Eng. Geol. Environ.* **71**, 263–268 (2012).
43. Parton, W. J. & Logan, J. A. A model for diurnal variation in soil and air temperature. *Agric. Meteorol.* **23**, 205–216 (1981).
44. Pruppacher, H. R., Klett, J. D. & Wang, P. K. Microphysics of clouds and precipitation. *Aerosol Sci. Technol.* **28**, 381–382 (1998).
45. Richter, D. & Simmons, G. Thermal expansion behavior of igneous rocks. *Int. J. Rock. Mech. Min. Sci. Geomech. Abstr.* **11**, 403–411 (1974).
46. Markewich, H. W. The nature of weathering: an introduction. *Soil Sci.* **147**, 152 (1989).
47. Walker, M. J. *Hot Deserts: Engineering, Geology and Geomorphology: Engineering Group Working Party report* (Geological Society, 2012).
48. Martel, S. J. et al. Effect of topographic curvature on near-surface stresses and application to sheeting joints. *Geophys. Res. Lett.* **33**, L01308 (2006).
49. Martel, S. J. Mechanics of curved surfaces, with application to surface-parallel cracks. *Geophys. Res. Lett.* **38**, L20303 (2011).
50. Stock, G. M., Martel, S. J., Collins, B. D. & Harp, E. L. Progressive failure of sheeted rock slopes: the 2009–2010 Rhombus Wall rock falls in Yosemite Valley, California, USA. *Earth Surf. Process. Landf.* **37**, 546–561 (2012).

51. Eberhardt, E., Stimpson, B. & Stead, D. Effects of grain size on the initiation and propagation thresholds of stress-induced brittle fractures. *Rock. Mech. Rock. Eng.* **32**, 81–99 (1999).
52. Hall, K., Guglielmin, M. & Strini, A. Weathering of granite in Antarctica: II. Thermal stress at the grain scale. *Earth Surf. Process. Landf.* **33**, 475–493 (2008).
53. Molaro, J. L., Byrne, S. & Langer, S. A. Grain-scale thermoelastic stresses and spatiotemporal temperature gradients on airless bodies, implications for rock breakdown. *J. Geophys. Res. Planets* **120**, 255–277 (2015).
54. Walsh, S. D. C. & Lomov, I. N. Micromechanical modeling of thermal spallation in granitic rock. *Int. J. Heat. Mass Transf.* **65**, 366–373 (2013).
55. Nara, Y., Yamanaka, H., Oe, Y. & Kaneko, K. Influence of temperature and water on subcritical crack growth parameters and long-term strength for igneous rocks. *Geophys. J. Int.* **193**, 47–60 (2013).

Acknowledgements

This research was supported by the National Natural Science Foundation of China (No.42202301).

Author contributions

C.W. performed program design and wrote the manuscript, C.L. contributed to the review and revision of the manuscript, J.W. and X.D. contributed to data management; X.Z. polished the manuscript.

Competing interests

The authors declare no competing interests.

Additional information

Correspondence and requests for materials should be addressed to Chengyu Liu.

Reprints and permissions information is available at <http://www.nature.com/reprints>

Publisher's note Springer Nature remains neutral with regard to jurisdictional claims in published maps and institutional affiliations.

Open Access This article is licensed under a Creative Commons Attribution-NonCommercial-NoDerivatives 4.0 International License, which permits any non-commercial use, sharing, distribution and reproduction in any medium or format, as long as you give appropriate credit to the original author(s) and the source, provide a link to the Creative Commons licence, and indicate if you modified the licensed material. You do not have permission under this licence to share adapted material derived from this article or parts of it. The images or other third party material in this article are included in the article's Creative Commons licence, unless indicated otherwise in a credit line to the material. If material is not included in the article's Creative Commons licence and your intended use is not permitted by statutory regulation or exceeds the permitted use, you will need to obtain permission directly from the copyright holder. To view a copy of this licence, visit <http://creativecommons.org/licenses/by-nc-nd/4.0/>.

© The Author(s) 2026